Data reconstruction at surface in immersed-boundary methods

Anand Bharadwaj S, Santanu Ghosh*

IIT-Madras, Chennai, Tamil Nadu 600036, India

ABSTRACT

This work compares interpolation techniques for data reconstruction at the surface in an immersed-boundary method. Three different methods of surface pressure reconstruction based on inverse distances are presented, which are christened as: Inverse Distance Weight (IDW) method, Inverse Distance Weight at Interpolation Point method (IDW-IP) and Inverse Distance Weight based on Upwinding (IDW-Upwind) method. Additionally, shear stress at the immersed surface is determined using two approaches: direct interpolation of velocity gradient at the surface using IDW method, and interpolation of velocity at a point along the surface normal using IDW-IP method. The interpolation methods are verified against analytic solutions of ideal flow past a circular cylinder and subsonic-supersonic inviscid flow in a convergent-divergent nozzle, and validated against laminar flow simulations of Mach 0.5 flow past a NACA0012 airfoil, Mach 2.0 flow past a circular cylinder, and Mach 3.0 flow past a 10° ramp. The verification cases show that while the pressure values reconstructed at the surface by the three interpolation methods are very similar for the incompressible flow, the IDW-Upwind method produces the sharpest pressure rise across the normal shock in the convergent-divergent nozzle. Comparisons of the reconstructed surface pressure coefficient (C_p) and skin-friction coefficient (C_f) with values available from literature or ANSYS-Fluent simulations conducted as part of the validation study show good match, but indicate that the reconstructed pressure and shear stress values at the immersed surface has noise, which, however, reduces with grid refinement. Further, the IDW and IDW-Upwind method for pressure reconstruction, and the gradient reconstruction based method for shear stress calculation are shown to produce less noise in computed values. Integrated drag and lift values using the reconstructed surface pressure and shear stress indicate that while the different methods used for pressure reconstruction result in similar values of aerodynamic loads, the gradient-based shear stress calculations result in more accurate load estimation. Finally, one of the interpolation methods (IDW-Upwind) is used to investigate the variation of the surface pressure coefficient with time for a NACA0012 airfoil undergoing non-periodic plunge motion in a Mach 0.2 flow. The computed surface pressure coefficients are correlated with the leading and trailing edge vortices in the flow field.

© 2019 Elsevier Ltd. All rights reserved.

1. Introduction

Immersed-Boundary Methods (IBMs) [1–11] comprise a technique of CFD in which flow past objects can be simulated without the need for the grid to conform to the surface of the object. This method, as such, decouples grid generation from the geometry of the body to a considerable extent, and allows the use of Cartesian or simple curvilinear grids. Immersed-boundary methods are useful for parametric studies [12–14], since they allow the re-use of the grid for different configurations of the geometry, for handling complex stationary/moving geometries [7,15–19] and fluid-structure interaction studies [20–22].

A challenge in this method is the accurate reconstruction of the pressure and shear stress (or heat flux) at the immersed surface. This becomes especially important if an IBM is to be used for fluid-structure interaction studies [20–22], for conjugate stress (or heat transfer) analysis of the immersed structure, or for comparison with experimental surface data. The normal and shear stress thus obtained at the immersed surface can also be integrated to compute the lift and drag forces as well as calculate moments. It is to be noted though that there are means other than the use of reconstructed data at the immersed surface, to calculate the integrated loads [19]. The distribution of the stresses (or heat flux) on the immersed surface, however, is not determined in the process of the load estimation in such cases.

In general, the approach for reconstructing data at the immersed surface will depend on the underlying IBM used. IBMs can be broadly classified into two categories based on the type

* Corresponding author.
E-mail address: sghosh1@ae.iitm.ac.in (S. Ghosh).

of forcing employed: continuous forcing based methods and discrete forcing based methods. While the former introduces a forcing term to the Navier–Stokes equations before discretization, as first proposed by Peskin [1], the latter introduces the forcing after discretization of the Navier–Stokes equations, in the cells near the immersed boundary (IB), as first proposed by Fadlun [3]. Implementation of discrete forcing IBMs are done typically by reconstructing the velocity field in fluid cells neighbouring the immersed boundary [7,8,23,24] or solid cells adjacent to the immersed boundary ([6,25,26]). The latter approach is referred to as the ghost-cell method.

In the case of continuous forcing IBMs, the discrete delta function used to interpolate the velocity at all the immersed surface points [1] can also used for the reconstruction of pressure (and other flow properties) at the immersed surface. However, these methods are restricted to thin (zero thickness) immersed objects that do not displace any fluid-volume, as rendered in the continuous forcing IB methods ([1,15,20,27]). It is important to note here that while the Lagrangian description of the immersed surface is sharp in this case, the Eulerian solution of the flow in such continuous forcing methods exhibit a diffused or smeared interface. Beyer & Leveque [28] applied Peskin's method to solve the 1-D heat flow between two phases with a forcing term, in which the interface between two phases was represented as an IB. In this case, the property from the grid points was interpolated onto a given IB point by using an interpolation method based on a discrete dirac delta function.

$$f(\alpha) = h \sum_j f(x_j) d_H(x_j - \alpha) \qquad (1)$$

where, h is grid spacing, $f(x_j)$ is property at the grid point j, α is the coordinate of the IB, and, d_H is the discrete representation of the dirac delta function.

In the case of discrete forcing methods, the underlying immersed-boundary is generally required to have a finite volume [3,25], and as such, realistic rendition of complex immersed boundaries, such as a human mannequin [7], and boundary-layer control devices [8,14,29] among others, can be done. However, the interpolation techniques have to be carefully constructed in this case for estimation of the surface properties. This is so, as such methods employ cell-classification for the fluid domain — interior and exterior to the immersed body—based on their position with reference to the (discretized) IB surface, with the majority [25,26,30] or all of the internal cells [7,8] having ad-hoc properties. Hence, the procedure for data interpolation at the IB needs to be selective in terms of the cells involved in interpolation, as internal cells having ad-hoc flow properties may not be used.

A cue for solution reconstruction at the immersed surface in such cases can be taken from the methods used to apply discrete forcing in cells immediately outside [7,8] or inside (internal cell) [3,6,25] of the immersed surface. For example, Majumdar et al. [30] proposed linear interpolation in a triangular domain, bi-linear interpolation in a rectangular domain, and linear-quadratic interpolation along tangential and wall-normal direction (all of which are polynomial based); however, this approach may not work in certain cases. To illustrate, Choi et al. [7] used a power-law based interpolation in the wall-normal direction for the forcing of the surface-parallel component of velocity, which can result in infinite values of shear strain rate at the immersed surface, and hence, cannot be used for estimation of shear stress.

In this work, different interpolation techniques, which use weights based on inverse distances, have been explored to reconstruct data at the immersed surface. The methods are designed to be used for any discrete forcing immersed-boundary method, whether sharp interface type [5,7,8,26] or otherwise [31,32], and are not dependent on the underlying discrete forcing algorithm

employed in the IBM. Specifically, three different interpolation procedures for reconstruction of pressure, and two methods for the estimation of shear stress at the IB surface have been used. While all of the methods use inverse-distance based interpolation in some form, they differ in detail, and one of the methods, the IDW-Upwind, is novel to the best knowledge of the authors.

The outline for the rest of the paper is as follows. The section Methodology discusses the details of the solver and the interpolation methods. The section Computational Details discusses the domain, grid details, and flow conditions for the verification and validation test cases. This is followed by the Results and Discussion section, wherein the results from the verification, validation and application studies are presented; the grid-convergence study for the simulations are also included in this section.

2. Methodology

A short description of the IBM used in this work is presented in this section. This is followed by more detailed descriptions of the interpolation methods presented in this work to reconstruct the data (pressure, shear stress) at the immersed surface and a brief description of the procedure used for integration of the surface loads. Body-fitted grid simulations have also been performed using ANSYS-Fluent for the validation cases of laminar flow past NACA 0012 airfoil and supersonic flow past a circular cylinder. A density-based steady solver using AUSM scheme for the convective fluxes, central difference scheme for the viscous fluxes and implicit time marching is used.

2.1. Immersed-boundary solver

The flow solver, REACTMB [33] is suitable for compressible laminar and turbulent flows with support for the immersed-boundary method [8]. This solver is a parallel, finite volume solver for structured grids that uses implicit (Crank–Nicolson scheme for unsteady simulations and Implicit Euler scheme for steady simulations) temporal integration for marching the Favre-averaged N–S equations in time. The inviscid fluxes at the cell faces are constructed using the Low Diffusion Flux Splitting scheme (LDFSS) [34] and viscous fluxes are constructed using a central difference type scheme. The Piece-wise Parabolic Method (PPM) [35] or MUSCL scheme [36] may be used for higher order extension in space. A local time-stepping is used to accelerate the convergence for steady state problems.

In the immersed-boundary method (of REACTMB) used herein [7,8], the cells of the grid are classified into three categories: field cells, band cells, and interior cells. A signed distance function is used to decide the category of a particular cell [7]. If the distance function is negative, it is classified as an interior cell; if the distance function is positive, and at least one of its neighbours is an interior cell, it is classified as a band cell. The rest of the cells with positive distance function are classified as field cells.

The immersed-boundary method uses a discrete forcing, first proposed by Fadlun et al. [3], which is done by suitable reconstruction of the solution in the band cells. To do this, first an *interpolation* point is constructed along the line normal to the surface point nearest to each band cell. This is done, as it is assumed that the near-surface (immersed body) properties are functions of the surface-normal coordinate only. The location of the *interpolation* point and its properties are determined by using inverse distance based interpolation of the position and data of the neighbouring cells. The wall-parallel component (relative to surface) of the velocity at the band cell is constructed using the interpolation point data and assuming a power law type distribution along the surface normal. The wall normal component of velocity is constructed by
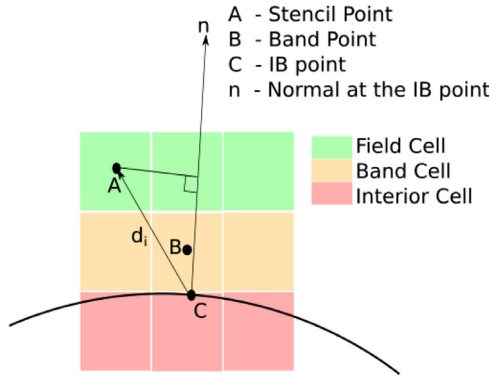
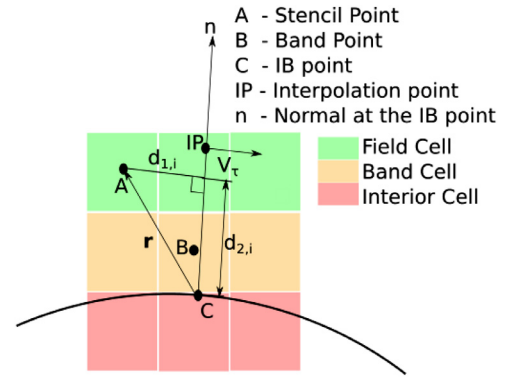**Fig. 1.** Schematic of interpolation stencil for IDW method.

Fig. 2. Schematic of interpolation stencil for IDW-IP method.

solving a discrete continuity equation near the surface. A more detailed description of the velocity reconstruction in the band cells is provided in Ghosh et al. [8]. Temperature in the band cells is reconstructed using Walz's formula for compressible boundary layers, and turbulence properties are constructed using law-of-the-wall type relations [8]. For determining density at the band cell, pressure is first reconstructed at the interpolation point, and the value is extrapolated to the band cell; the density is then determined using this pressure, the reconstructed value of temperature at the band cell, and the equation of state.

2.2. Interpolation methods (Pressure)

The basic premise of the solution reconstruction at the immersed surface involves the construction of a stencil around each IB point that includes at least one field cell. In order to build the stencil, the nearest cell-centre to the IB point is determined. Subsequently, the neighbouring cells (that share at least one vertex with the nearest cell) are considered. This is the smallest stencil used and is of dimension 3×3 cells in 2D. In case this stencil does not include at least one field cell, it is expanded by one cell size in all directions giving rise to a 5×5 stencil. This procedure is continued until at least one field cell is available in the stencil. Once the stencil has been fixed, the data at field and band cells of the stencil are used to reconstruct the value at the IB point. The interpolation techniques, as applied to pressure data, are discussed next.

2.2.1. Inverse distance weight (IDW)

In this method, once the stencil is built, the inverse of the distance (d_i, in Fig. 1) between the centre of every field/band cell ('A') of the stencil and the IB point ('C') is used as a weight to determine the value of pressure at the IB point, as given below.

$$P_{IB} = P_C = \frac{\sum_i P_i / d_i^m}{\sum_i 1 / d_i^m} \tag{2}$$

where i sums over all the field and band cells of the stencil.

Different values of m (> 1) may be chosen to perform this interpolation; the effect of the cells relatively far from the IB point, on the interpolated value drops as m increases. However, the effect of the value of m on the results was found not to be very significant. Hence, a value of $m = 1$ has been used in all the applications of this method.

2.2.2. Inverse distance weight at interpolation point method (IDW-IP)

Interpolation Point (IP) [7] is defined, in this context, as a point, which lies on the normal (to immersed surface) at the IB point, at which the properties are interpolated from the surrounding cells, and subsequently transferred to the IB point. There are two aspects that need to be determined about the interpolation point:

firstly, its location, and secondly, its properties. To determine the location of the interpolation point, the following relation is used, as outlined in Choi et al. [7].

$$d_{IP} = \frac{\sum_i d_{2,i} / d_{1,i}}{\sum_i 1 / d_{1,i}} \tag{3}$$

Here, d_1 is the perpendicular distance from 'A' to the normal at the IB point, and d_2 is the projection of the distance from 'A' to the IB point, along the normal at the IB point, as illustrated in Fig. 2. To determine the value of pressure at the interpolation point, the following relation is used.

$$P_{IP} = \frac{\sum_i P_i / d_{1,i}}{\sum_i 1 / d_{1,i}} \tag{4}$$

In this approach, the pressure determined at the interpolation point is copied to the IB point. This method can also be used for a higher order reconstruction of pressure at the IB point [7].

2.2.3. Inverse distance weight based on upwinding (IDW-Upwind)

In this method, in addition to the distance, the flow direction relative to the IB and Mach number are considered to determine the interpolation weights. This is a novel approach, to the best knowledge of the authors, that combines distance and Mach number to estimate the interpolation weights. The formulation is adapted from the upwind-biased reconstruction of pressure flux at cell interfaces in finite-volume methods proposed by van Leer [37], which makes use of Mach number based polynomials. In this case, the surface normal at the IB point is considered as an interface with information coming from the upstream and downstream directions. The pressure at this interface is then interpolated at the IB point using Mach number and distance based weights. The interpolated pressure at the IB point is calculated in this case as:

$$P_{IB} = P_c = \frac{\sum_i P_i w_i}{\sum_i w_i} \tag{5}$$

where w_i is the weight associated with the ith cell-centre of the stencil.

The weights w_i are given by:

$$w_i = \frac{(1 + |M_i|)^2 (2 - |M_i|)}{4d_i}, \text{ for } |M_i| \leq 1 \text{ and } \vec{V}_i . \vec{r}_n < 0$$

$$w_i = \frac{(1 - |M_i|)^2 (2 + |M_i|)}{4d_i}, \text{ for } |M_i| \leq 1 \text{ and } \vec{V}_i . \vec{r}_n > 0$$

$$w_i = \frac{1}{d_i}, \text{ for } |M_i| > 1 \text{ and } \vec{V}_i . \vec{r}_n < 0$$

$$w_i = 0, \text{ for } |M_i| > 1 \text{ and } \vec{V}_i . \vec{r}_n > 0 \tag{6}$$

Here the Mach number M_i is based on the component of velocity perpendicular to the normal (V_n) and the local speed of sound;
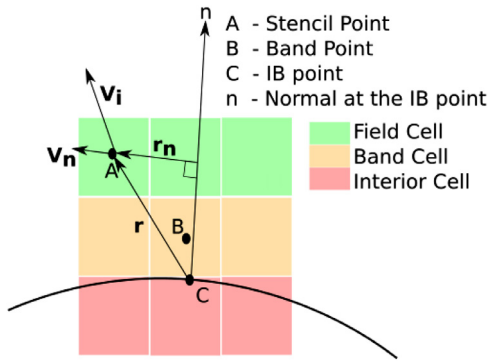
Fig. 3. Schematic of interpolation stencil for IDW-Upwind method.

Table 1
Simulation details.

Immersed surface	$i_{max} \times j_{max} \times k_{max}$	δ_{min} (m)	M	Re	α
NACA0012 airfoil	$4512 \times 900 \times 1$	5E−4	0.5	5000	1^0
Circular cylinder	$1360 \times 980 \times 1$	4E−3	2.0	300	–
10° Ramp	$1024 \times 576 \times 1$	2E−3	3.0	16800	–
NACA0012 airfoil (plunge)	$780 \times 1400 \times 1$	1.0E−3	0.2	1000	0^0

also, d_i is the distance between the field/band cell-centre ('A') and the IB point, 'C' (In Fig. 3, $d_i = |\vec{r}|$). The sign of the dot product of the velocity vector at the cell-centre and the vector $\vec{r}_n$ i.e. $\vec{V}_i.\vec{r}_n$, is found in order to determine the orientation of the flow at the cell-centre relative to the normal at the IB point 'C'. If the dot product is negative, the local flow is towards the normal; if it is positive, the local flow is away from the normal. The interpolation weights are constructed such that they result in higher weights for cell-centres having flow towards the surface normal than those having flow away from the normal, even when they are at identical distances from the IB point. Thus, the interpolation weights can be considered as upwind biased, as they are sensitive to the local direction of flow and have greater influence of the local upstream as compared to the local downstream.

There may be a situation where all the field cells in the stencil have $|M_i| > 1$, and the velocity vector at the field cell points away from the normal. In such a case, the weights (w_i) for all the cells in the stencil would be zero. If this happens, the stencil size is increased to ensure there exists at least one field cell with a non-zero weight.

2.3. Interpolation of shear stress

Two different approaches are used to determine the shear stress at the immersed surface; these are described in the following paragraphs.

2.3.1. Velocity reconstruction at IP using IDW-IP
In order to determine shear stress at an IB point, the fluid velocity is first reconstructed at the interpolation point ($\vec{V}_{IP}$ in Fig. 2) using the IDW-IP method. The component of $\vec{V}_{IP}$ perpendicular to the normal, and hence parallel to the immersed surface ($\vec{V}_\tau$) is then determined, and the shear stress at the IB point is calculated as,

$$\tau_w = \mu_w \frac{|\vec{V}_\tau|}{d_{IP}} \tag{7}$$

where, μ_w is the dynamic viscosity and d_{IP} is given by Eq. (3). The method adopted here is simplistic and is expected to under predict the shear stress at the surface. This is because the shear stress calculation, as given in Eq. (7), implicitly assumes a linear variation of wall parallel velocity between the surface and the interpolation point, which can introduce large errors if the interpolation point location is not sufficiently close to the surface.

2.3.2. Velocity gradient reconstruction at surface using IDW
In this case, the velocity gradient is first computed in the cells comprising the interpolation stencil and then reconstructed at the immersed-boundary point using weights defined by the IDW method, wherein Eq. (4) is used by replacing pressure with

the scalar components of the velocity gradient tensor. The reconstructed velocity gradient at the immersed surface is then used to determine the viscous stress tensor at the surface.

2.4. Calculation of aerodynamic forces

The integrated loads, lift and drag, are obtained using the reconstructed surface values of pressure and shear stress at the IB points, and the geometry of the line elements, which are line segments connecting two adjacent IB points. The average pressure and shear stress for each element are determined by simply averaging the values at its two end nodes or IB points. The unit normal vector to the line segment is then used to determine the orientation of the pressure force, and the shear stress is considered to act along the line element. The forces on each element are then summed up vectorially over the entire IB surface to get the total forces. The net lift force as such has some contribution from the shear stresses, and drag is due to both shear stress (skin-friction) and pressure distribution (form drag).

3. Computational details

The free-stream conditions and grid sizes for the different simulations - except the verification cases, which did not include any flow simulation, are listed in Table 1. The grid sizes listed here are arrived at from grid resolution studies that are discussed in Section 4. The number of points rendering the IB in all cases is decided such that the cells intersected by the IB contain at least 3–4 IB points.

3.1. Verification

The aim of this study is to estimate the performance of the pressure reconstruction methods using exact/analytic solutions and not results from CFD simulation, such that any errors in the reconstructed surface pressures can be attributed only to the interpolation procedure. The exact pressure values are populated at discrete locations - cell centres of a Cartesian grid – which are then used to determine the pressure at the immersed surface using the reconstruction methods outlined in Section 2. The reconstructed values of pressure are then compared with the exact solution.
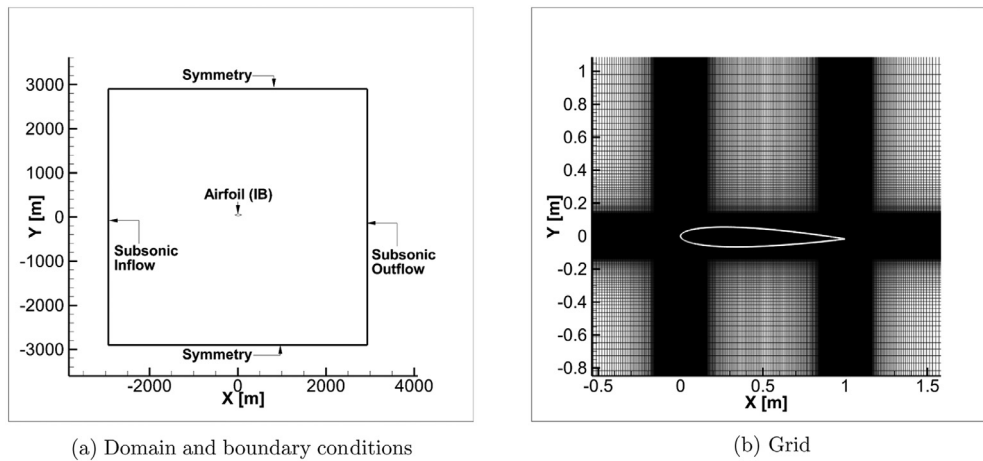
3.1.1. Ideal flow past a circular cylinder
For this case an exact solution, derived from potential flow theory, exists, which is used to compare with the reconstructed values of pressure on the surface of the cylinder. A square domain tessellated using Cartesian grids is used, which contains the immersed object: the circular cylinder, which is rendered using a cloud of points. Three grids are used, with each successive refined grid having four times the number of cells as its predecessor.

The error in the estimation of the integrated lift force, which should actually be zero, is used to estimate the order of accuracy of the interpolation methods.

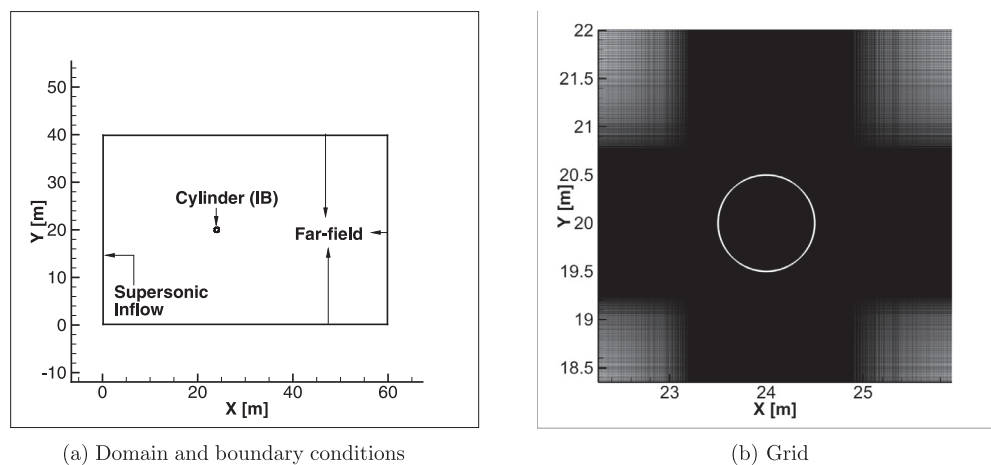#### 3.1.2. Quasi-one-dimensional flow through a convergent-divergent nozzle
The pressure distribution for a quasi-one-dimensional flow through a convergent-divergent nozzle is obtained by applying

(a) Domain and boundary conditions

(b) Grid

Fig. 4. Validation study: Mach 0.5 laminar flow past a NACA0012 airfoil.

(a) Domain and boundary conditions

(b) Grid

Fig. 5. Validation study: Mach 2.0 laminar flow past a circular cylinder.

isentropic relations and normal-shock relations. The plenum pressure is 6894.76 Pa, and the exit pressure is set to 5171.07 Pa. The total temperature of the plenum is 55.56 K. The domain ranges from $x = 0$ m to $x = 10$ m, with the throat situated at $x = 5$ m. The areas before and after the throat are given by:

$$A_{pre-throat} = 1.75 - 0.75cos(\pi(0.2x - 1.0))$$

$$A_{post-throat} = 1.75 - 0.25cos(\pi(0.2x - 1.0))$$

For the aforementioned conditions, there is a stationary normal shock that forms at $x = 7.55$ m. This test case is, as such, suitable for testing the performance of the pressure interpolation methods in the presence of both smooth variation and discontinuities in pressure. The center-line of the convergent-divergent nozzle is discretized into equally spaced grid points, where the exact solution is populated, and IB points, wherein the pressure is to be interpolated. It is ensured that the grid points and IB points are not collocated. The exact solution stored at the grid points is then used to interpolate the pressure values at the IB points using the pressure interpolation methods discussed in Section 2.2.

3.2. Validation: Mach 0.5 laminar flow past a NACA0012 airfoil

The domains along with the boundary conditions are shown in Fig. 4a. Subsonic inflow condition (velocity is fixed, pressure is ex-

trapolated) and subsonic outflow (velocity is extrapolated, pressure is fixed) are used at the left and right faces respectively. A symmetry boundary condition is used at the top and bottom faces of the domain as these are far away (≈ 3000 c) from the airfoil surfaces and the flow can be assumed to be approximately parallel to the free-stream.

Fig. 4b shows a representative grid for the simulation of flow past the NACA0012 airfoil. As seen in the figure, the grid is dense in the vicinity of the airfoil in order to capture the flow gradients accurately. For the airfoil simulations, an inner box, which contains the airfoil, having constant spacing (δ_{min}) along X and Y directions is used. The grid stretches out using a *tanh* function towards the outer parts of the domain starting from the edges of the inner box. The leading edge of the airfoil is at origin and the chord length is unity.

In addition to the IB simulations, a solution on a body-fitted grid is obtained using ANSYS-Fluent. The simulation was performed on a fine, structured C-grid provided in '2nd International Workshop on High-Order CFD Methods' [38]. The grid contains 35,840 cells, and is the second finest grid in the series of grids provided in the workshop, with the C-boundary having the velocity-inlet boundary condition and the rest of the boundaries, having pressure-outlet boundary condition. The C_p and C_f values extracted from this simulation are used to compare with the corresponding reconstructed quantities from the IB simulations.
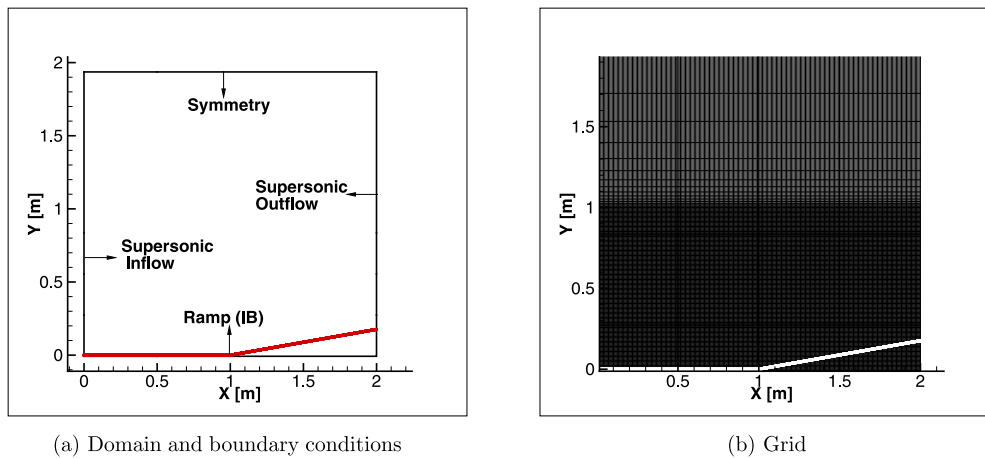
(a) Domain and boundary conditions

(b) Grid

Fig. 6. Validation study: Mach 3.0 laminar flow past a 10° ramp.

(a) Domain and boundary conditions

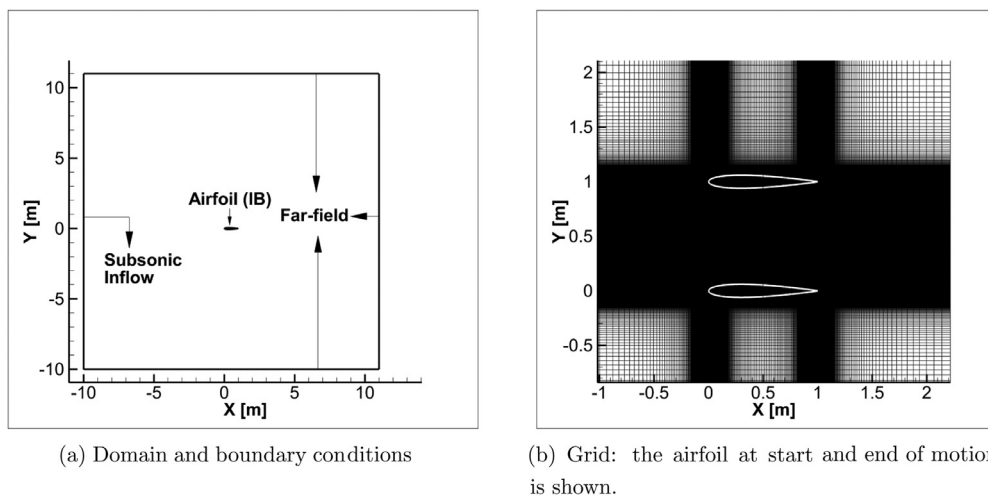(b) Grid: the airfoil at start and end of motion is shown.

Fig. 7. Mach 0.2 laminar flow past a plunging NACA0012 airfoil.

Table 2
Data interpolation at immersed surface: list of parameters.

Pressure reconstruction	Shear stress reconstruction	Method label
IDW	Velocity reconstruction at IP	A1
IDW-IP	Velocity reconstruction at IP	A2
IDW-Upwind	Velocity reconstruction at IP	A3
IDW	Velocity gradient reconstruction at surface	A4
IDW-IP	Velocity gradient reconstruction at surface	A5
IDW-Upwind	Velocity gradient reconstruction at surface	A6

3.3. Validation:Mach 2.0 laminar flow past a circular cylinder

The domain and boundary conditions for this test case is shown in Fig. 5a. A far-field boundary condition is used on all faces except for the left face, wherein a supersonic inflow (conditions prescribed) boundary condition is used. In Fig. 5b a dense uniform mesh embeds the cylinder and stretches out in both X and Y directions towards the domain boundaries. The center of the cylinder is at (24 m, 20 m) and the diameter is 1 m. A Fluent simulation has been computed in this case also to generate C_f data for comparison with the reconstructed C_f from the IB simulation.

3.4. Validation: Mach 3.0 flow past a 10° ramp

The domain and boundary conditions for this test case is shown in Fig. 6a. A supersonic inflow condition is used at the left or inlet face, a symmetry boundary condition is used at the top face and a supersonic outflow boundary condition is used at the right or exit face. In Fig. 6b a dense uniform mesh embeds the ramp and stretches out in Y direction. The ramp starts at $X = 1.0$ m and is rendered as an IB.

The primary motivation for this test case is to compare the surface pressure coefficients for the different interpolation methods in the presence of a shock. The comparison is made only with data available from literature [39] in this case.

3.5. Application: Mach 0.2 flow past a plunging NACA0012 airfoil

Fig. 7a shows the domain used for the simulations. A subsonic inflow boundary condition is used in this case with a far-field boundary condition imposed at the other boundaries. The grid zoomed in near the airfoil shows the presence of an inner box with
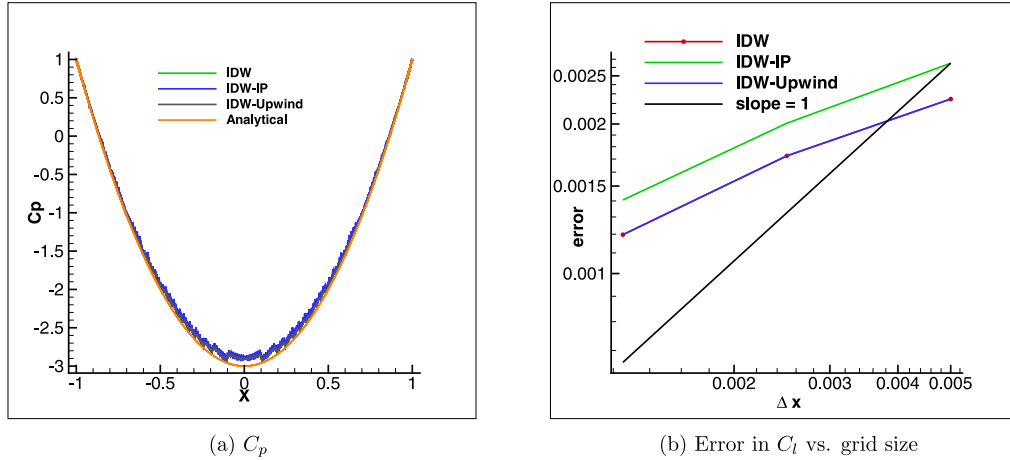
(a) C_p (b) Error in C_l vs. grid size

Fig. 8. Verification of surface-data interpolation for inviscid, incompressible flow past a circular cylinder.

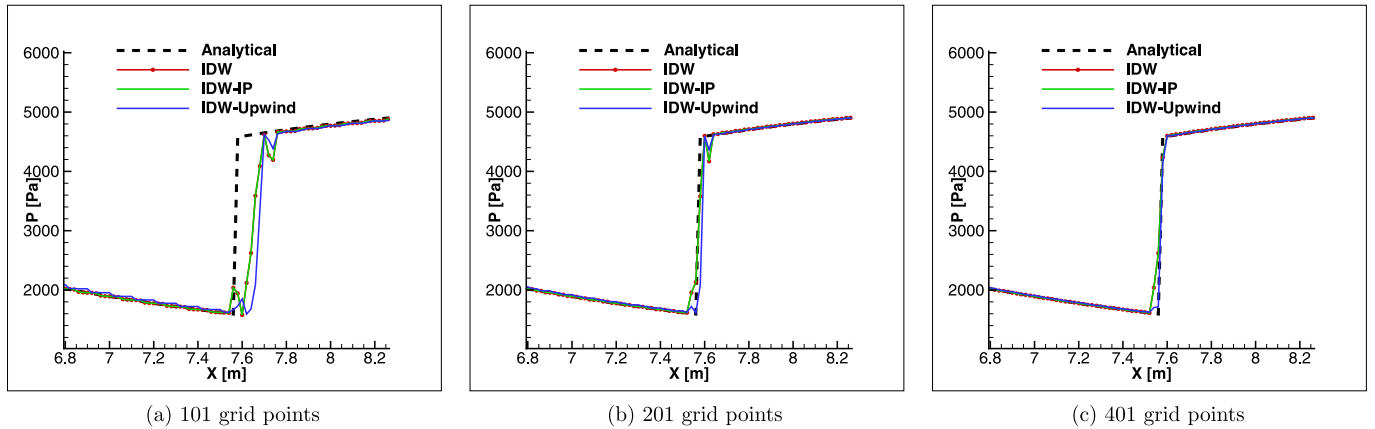(a) 101 grid points   (b) 201 grid points   (c) 401 grid points

Fig. 9. Interpolated pressure distribution in a CD nozzle with pressure ratio 0.75.

a dense grid. The inner box is sized in this case to accommodate the airfoil throughout the plunge motion. The point clouds representing the NACA0012 airfoil at its starting and ending positions are also shown in Fig. 7b. The chord length and the plunge distance are both equal to 1m. The plunge motion of the airfoil is given by the following equation [40].

$$h(t) = 0.25t^2(3 - t) \tag{8}$$

where $h(t)$ is the vertical displacement of the airfoil in metres and t is the time in seconds. The total time for the heaving motion is 2s, during which the airfoil moves up by 1m.

4. Results and discussion

A list of the choices of methods for pressure and shear-stress reconstruction at the immersed surface used in this work is presented in Table 2. The verification test cases are presented first, followed by the validation test cases and finally the application of the data reconstruction methods for flow past a plunging NACA0012 airfoil is presented. A grid/time-resolution study is also included here for the test cases. The interpolation parameters (method and stencil) used for the grid-resolution study is listed in Table 3.

The studies include simulations on three levels of grid, starting from the finest mesh. The coarse meshes were generated by removing alternate grid points along the X and Y directions, starting with the finest mesh. Further, using the calculated C_d values for the three grids the observed order of convergence [41], p, and *exact*

Table 3
Interpolation parameters for grid convergence study.

Immersed surface	NACA0012 airfoil/Circular cylinder
Pressure interpolation	IDW-Upwind
Shear stress interpolation	Velocity gradient reconstruction at surface
Method Label	A6
Stencil	3×3

value using Richardson extrapolation, $C_{d,ref}$, are calculated. In order to check for solution convergence with grid resolution, C_p and C_f plots are compared, and the error in C_d, $\Delta C_d (= C_d - C_{d,ref})$, is also determined, as percentage of $C_{d,ref}$ for the simulations of flow past NACA0012 airfoil and circular cylinder. For the Mach 3.0 flow past the ramp, only C_p plots are used for checking grid convergence. It is to be noted that errors in C_p, C_f and C_d are also a property of the discrete solution obtained using the immersed-boundary approach and not just the interpolation methods (IDW, IDW-IP, and IDW-Upwind) used.

4.1. Verification

4.1.1. Ideal flow past a circular cylinder
Fig. 8a shows the variation of the coefficient of pressure with X along the upper surface of the circular cylinder. The results indicate that IDW, IDW-IP, and IDW-Upwind methods have almost identical predictions of the surface pressure, and that the error in the prediction increases as one approaches the top of the cylinder
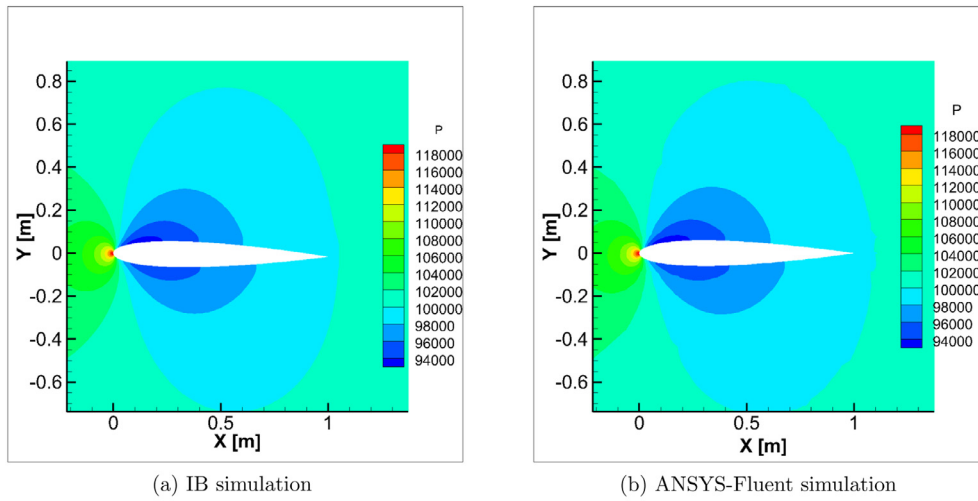
(a) IB simulation   (b) ANSYS-Fluent simulation

Fig. 10. Static gauge pressure contours for Mach 0.5 flow past NACA0012 airfoil.

(a) C_p plot near leading edge (zoomed-in)   (b) C_f plot   (c) Error in C_d vs. grid spacing
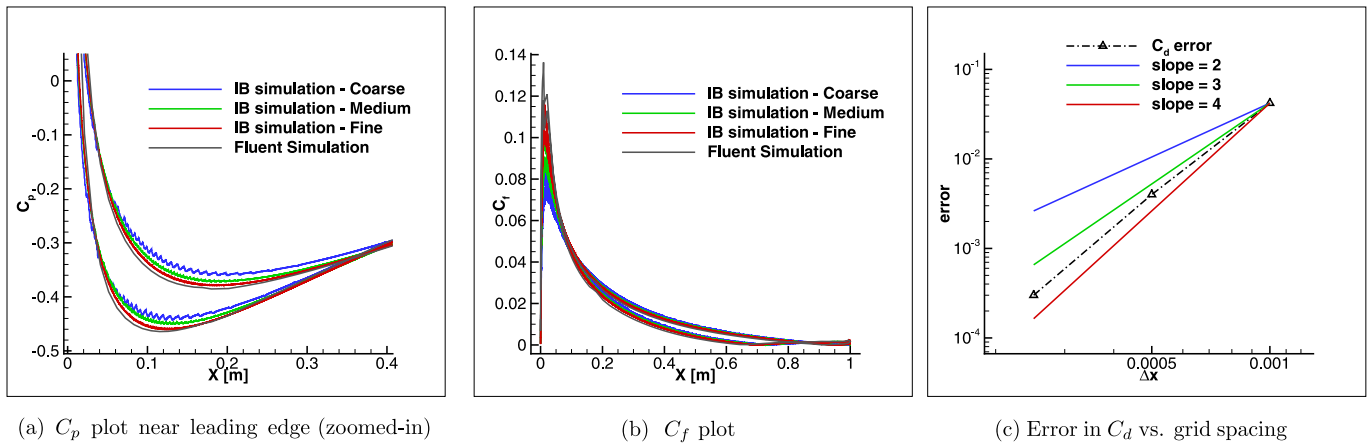
Fig. 11. Grid-convergence study for simulation of Mach 0.5 flow past NACA0012 airfoil.

(a) IDW   (b) IDW-IP   (c) IDW-Upwind
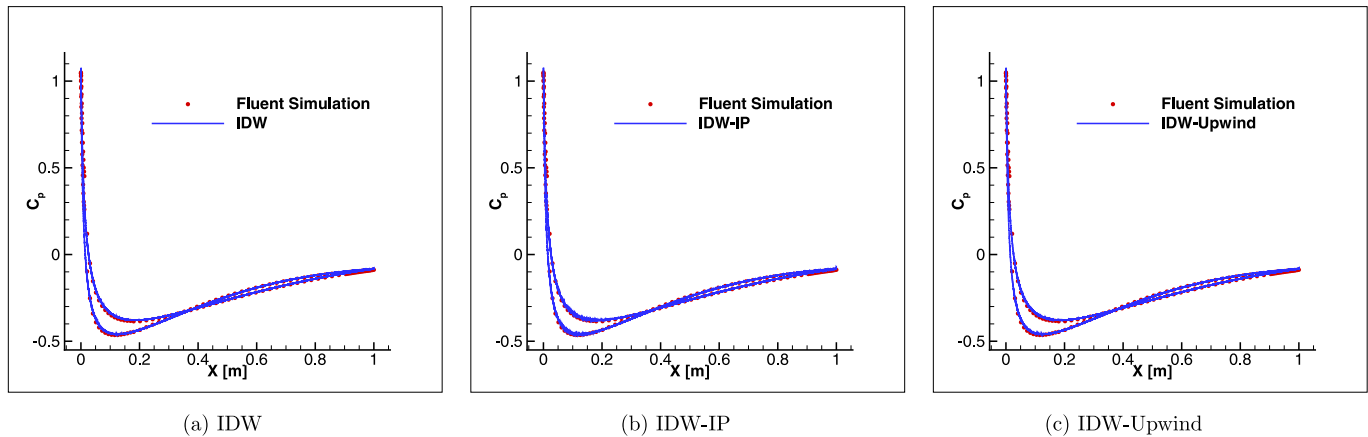
Fig. 12. Comparison of interpolation pressure reconstruction methods using 3×3 stencil for Mach 0.5 flow past NACA0012 airfoil.

(point of minimum pressure). The variation of the integrated lift force for the three methods are compared in Fig. 8b. As the lift force should be zero, this also shows the error in the prediction of the integrated force with grid refinement. It is observed that the IDW and IDW-Upwind methods have almost identical errors, while the IDW-IP method has a higher error. The errors reduce with grid refinement as expected.

4.1.2. Quasi-one-dimensional flow through a convergent-divergent nozzle

Fig. 9 compares pressure interpolated by each of the three pressure interpolation methods with the analytic solution, for three grids with 101, 201 and 401 equally spaced points on the centre-line; the IB consists of 501 equally spaced points. It is seen that for all three grids, the IDW-Upwind method captures
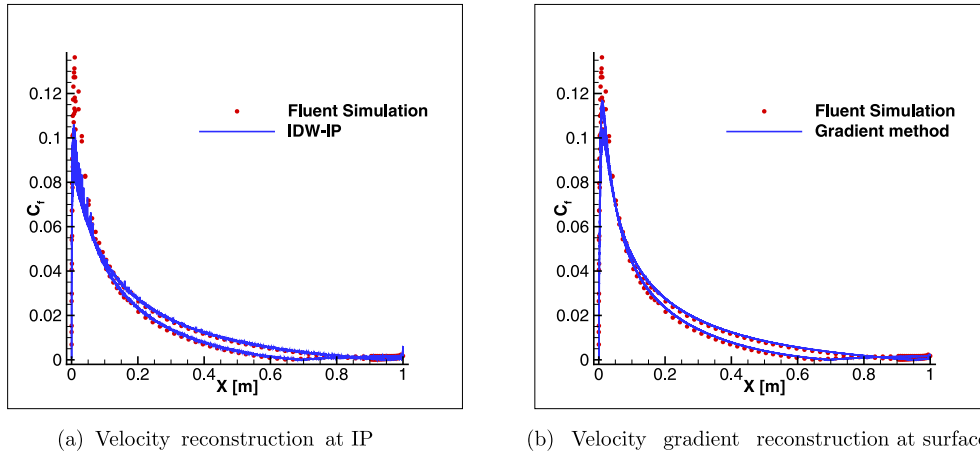
(a) Velocity reconstruction at IP

(b) Velocity gradient reconstruction at surface

Fig. 13. Comparison shear-stress reconstruction methods using 3×3 stencil for Mach 0.5 flow past NACA0012 airfoil.

(a) C_p using IDW-UP
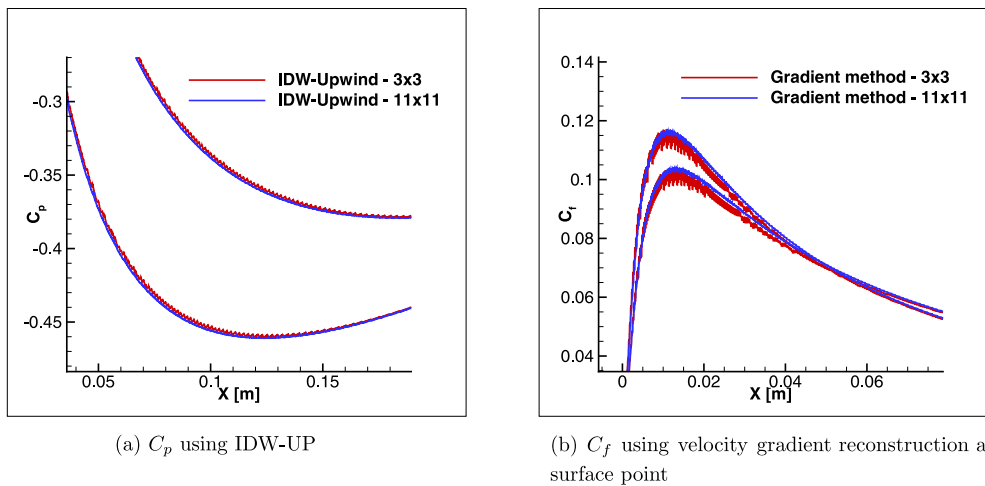
(b) C_f using velocity gradient reconstruction at surface point

Fig. 14. Effect of stencil size on surface pressure and skin-friction coefficients for Mach 0.5 flow past NACA0012 airfoil.

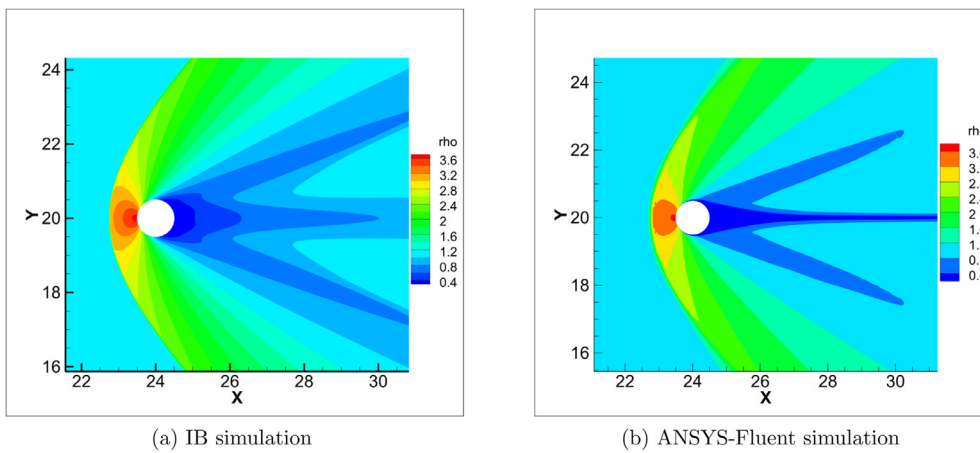(a) IB simulation

(b) ANSYS-Fluent simulation

Fig. 15. Density contours of Mach 2.0 flow past circular cylinder.

a sharper shock compared to the other two methods. Additionally, it is seen that the noise in the immediate downstream region of the shock has lower peaks in the case of IDW-Upwind method, as compared to the other two methods. In the regions of smooth pressure variation, all three methods perform equally well. It is to be noted that in real flows, such sharp discontinuities in flow variables may not appear on walls due to the presence of the boundary layers. In such situations, as such, all the three

pressure reconstruction methods are expected to provide similar results.

4.2. Validation: Subsonic laminar flow past NACA0012 airfoil

Fig. 10 shows the comparison of static pressure contours between the IB simulation and the ANSYS-Fluent simulation. The grid for the simulation on ANSYS-Fluent was obtained from the
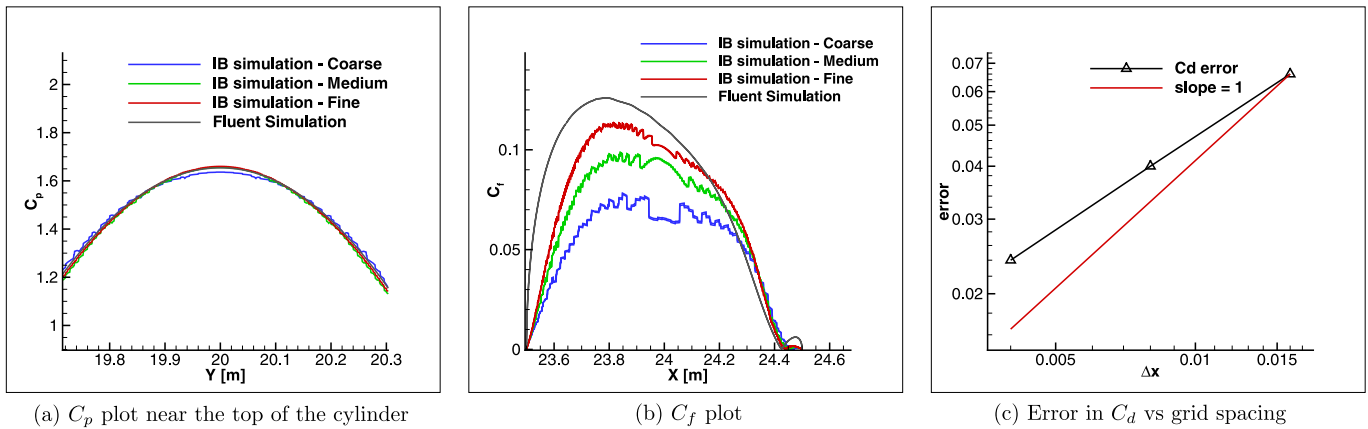
(a) C_p plot near the top of the cylinder (b) C_f plot (c) Error in C_d vs grid spacing

Fig. 16. Grid-convergence study for Mach 2 supersonic flow past a circular cylinder.
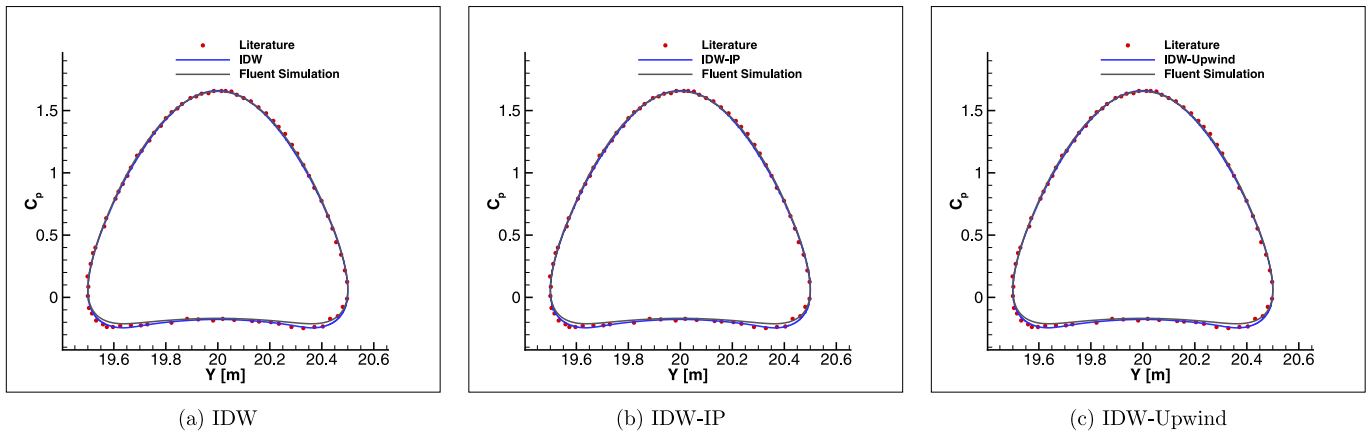

(a) IDW (b) IDW-IP (c) IDW-Upwind

Fig. 17. Comparison of pressure interpolation methods using 3 × 3 stencil for Mach 2.0 flow past circular cylinder.

Table 4
Comparison of C_l and C_d values for Mach 0.5 flow past NACA0012 airfoil (A1:A6) ; $C_{l,lit} = 1.8273e\text{-}2$, $C_{d,lit} = 5.531e\text{-}2$.

Interpolation method	C_l (error)	C_d (error)
A1	1.90e-2 (4.09%)	5.25e-2 (−5.04%)
A2	1.90e-2 (4.03%)	5.26e-2 (−4.99%)
A3	1.90e-2 (4.03%)	5.25e-2 (−5.01%)
A4	1.87e-2 (2.12%)	5.36e-2 (−3.02%)
A5	1.87e-2 (2.06%)	5.37e-2 (−2.97%)
A6	1.87e-2 (2.06%)	5.37e-2 (−2.98%)
ANSYS-Fluent	1.85e-2 (1.2%)	5.693e-2 (2.9%)

Table 5
Comparison of C_l and C_d values for Mach 0.5 flow past NACA0012 airfoil (A1-A6); $C_{l,lit} = 1.8273e\text{-}2$, $C_{d,lit} = 5.531e\text{-}2$.

| Interpolation	δ error (C_l)	δ error C_d
A1	−0.71%	−1.23%
A2	−0.60%	−1.18%
A3	−0.49%	−1.46%
A4	−0.71%	−0.42%
A5	−0.55%	−0.40%
A6	−0.44%	−0.67%

higher order workshop [38]. The grid for the IB simulation is listed in Table 1. The contour plots look very similar indicating that the flow field predicted by the two simulations agree qualitatively.

4.2.1. Grid refinement

The C_p and C_f plots for the simulations using the three grids are shown in Fig. 11. Fig. 11a shows a zoomed in view of C_p plots wherein it is clear that the C_p predictions on the finest and medium grid are very close to each other and approach the results of the ANSYS-Fluent simulation. Further, the noise in the reconstructed pressure decreases with increase in grid resolution, which is expected. Similar observations about noise in the reconstructed values can be made about the C_f plot shown in Fig. 11b. The accuracy of the reconstruction also improves, especially near the leading edge, with grid refinement. Fig. 11c shows the convergence in the error with grid refinement. The value of C_d calculated using Richardson's extrapolation is 5.368 e-02 and the observed order of convergence, p, in this case is equal to 3.22.

4.2.2. Variation in interpolation method

Fig. 12 shows the C_p plots obtained from the three pressure reconstruction methods (Section 2.2) that use the smallest stencil. The three methods agree very closely with each other and with the body fitted grid simulation of ANSYS-Fluent. Fig. 13 plots the skin-friction coefficient using the two shear-stress reconstruction methods (Section 2.2.3) for the smallest stencil. It can be observed that the shear stress reconstruction that makes use of the velocity interpolation using IDW-IP has more noise than the gradient-based method. This is possibly due to the inherent smoothing present in the gradient-based method, as it involves a larger effective stencil for interpolation of the shear stress. This is so, as the calculation of the velocity gradients in the cells of the smallest 3 × 3 stencil requires the use of data from the adjacent neighbours, which
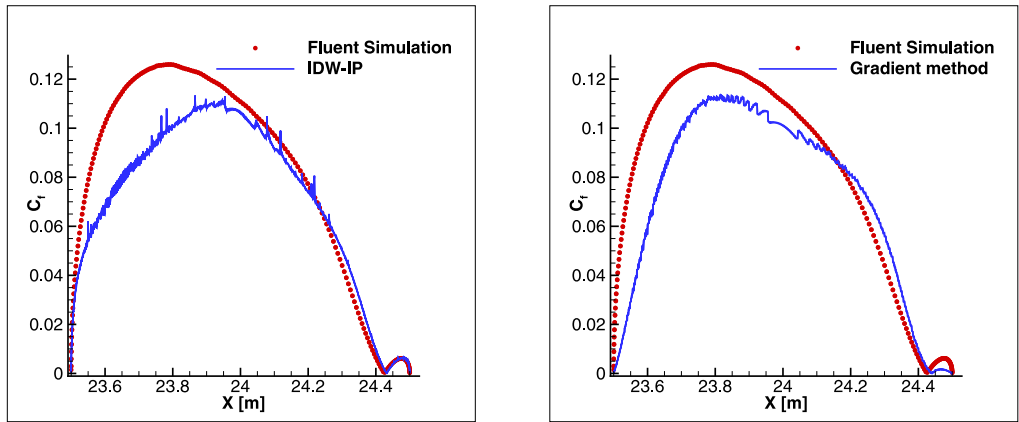
(a) Velocity reconstruction at IP using IDW-IP

(b) Velocity gradient reconstruction at the surface

Fig. 18. Comparison of shear-stress reconstruction methods using 3×3 stencil for Mach 2.0 flow past circular cylinder.
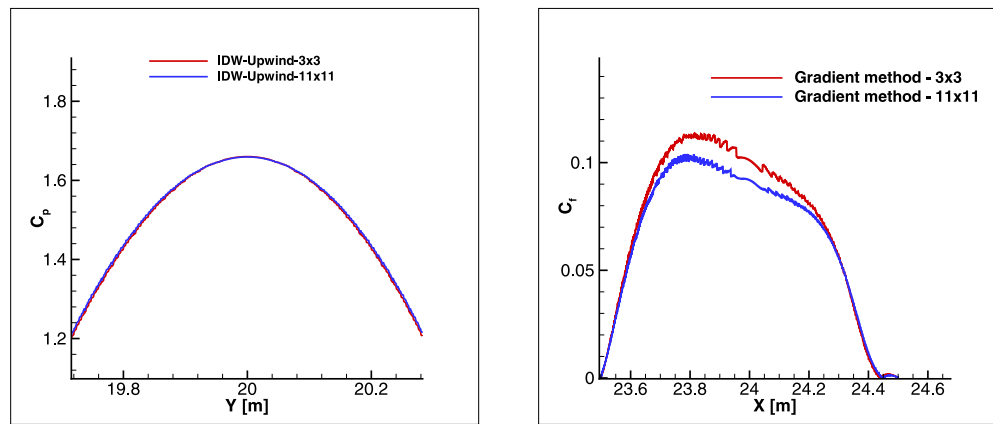
(a) C_p using IDW-Upwind

(b) C_f using velocity gradient reconstruction

Fig. 19. Effect of stencil size on surface pressure and skin-friction coefficients for Mach 2.0 flow past a circular cylinder.
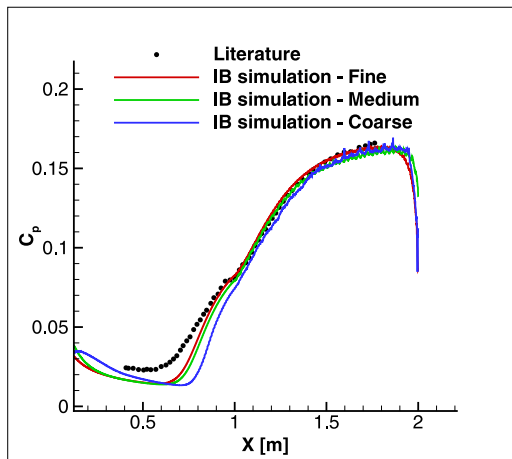

Fig. 20. C_p plot comparison across grids for Mach 3.0 flow past a 10° ramp.

effectively increases the size of the interpolation stencil. The results from both the methods show very good agreement with literature.

C_l and C_d values are also tabulated in Table 4, in which the values in parenthesis denote the error, which is calculated relative to a reference value obtained from literature [38], and expressed as a percentage of the reference value. It is observed from Table 4 that the lift and drag coefficients obtained using the IBM simulation

and subsequent interpolations using methods A1–A6 are within 5% of the values reported in literature. It is interesting to note that predictions of both lift and drag coefficients improve with the use of velocity gradient reconstruction at the surface for the shear stress calculation. The results indicate that while the accuracy of the integrated loads are not affected by the choice of pressure reconstruction methods proposed in this work, it is more accurate with the use of the velocity gradient based approach for the shear stress reconstruction, for the choice of a 3×3 interpolation stencil.

4.2.3. Variation in stencil size

The effect of having a larger stencil size has a smoothing effect on the surface data in all three cases of pressure interpolation. Fig. 14a shows the comparison of the IDW-Upwind method for two different stencil sizes: 3×3 and 11×11. This behaviour can be explained as follows: physically, the steady state solution at any point in the domain is dependent on the solution at all other points in the domain, the flow being steady and subsonic; a larger interpolation stencil results in more cells affecting the interpolated value, which captures the physics better and has a smoothing effect. However, this may not be true for flows with shocks in which case, a larger stencil size may result in more noise in the interpolated data. A similar effect is observed for the shear stress reconstruction methods and is shown here for the case wherein the velocity gradient is interpolated at the surface in Fig. 14b.

Table 5 compares the values of C_l and C_d computed with the 3×3 and 11×11 interpolation stencils. The difference in the
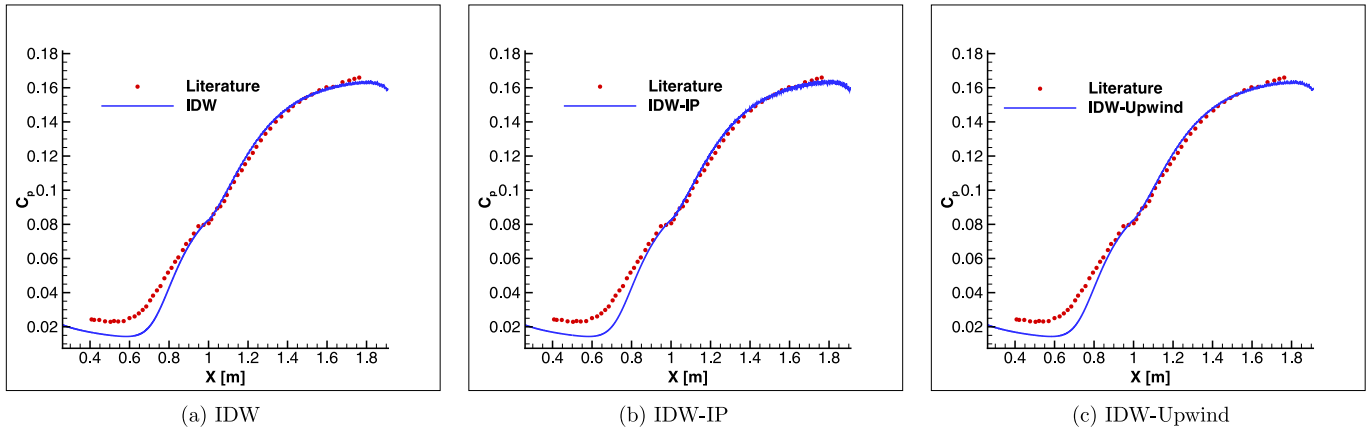
Fig. 21. Comparison of pressure interpolation methods using 3 × 3 stencil for Mach 3.0 flow past a 10° ramp.
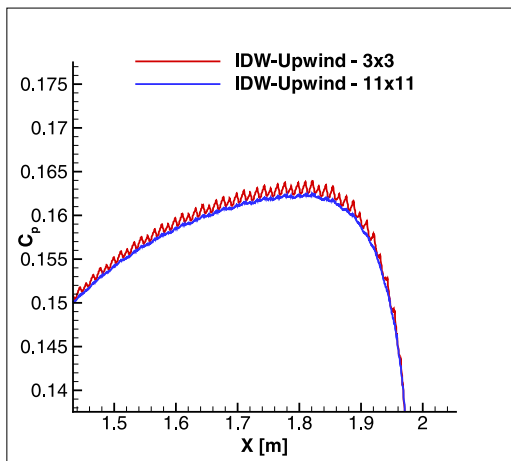

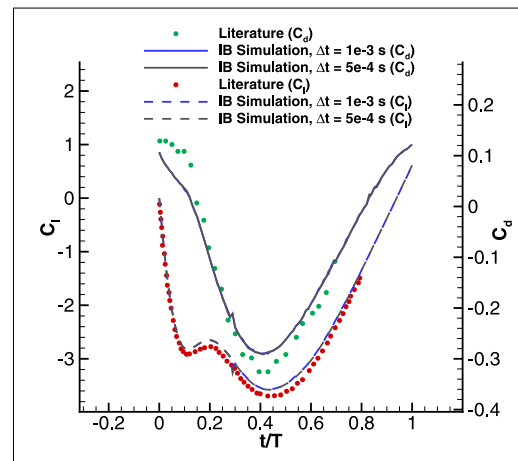**Fig. 22.** Comparison of C_p using IDW-Upwind, for different stencils.

Fig. 23. Temporal convergence study for Mach 0.2 flow past plunging NACA0012 airfoil.

absolute value of the errors in lift and drag coefficients for the two cases - corresponding to the two different sized interpolation stencil – is reported here. A negative value is to be read as a reduction in error while a positive value indicates an increase in error. It is seen from the tabulated values that increasing the stencil, uniformly produces a reduction in the error for both lift and drag coefficients. However, although the lift predictions change by similar values across all methods of interpolation, the change in drag is very different for the two different choices of shear stress calculation; the shear stress determination using the velocity reconstruction at the inteprolation point is observed to be more sensitive to the interpolation stencil in this case. Among the pressure interpolation methods, it is observed that while the IDW method shows the highest improvement in C_l prediction, the IDW-UP method produces the most improvement in the C_d prediction.

4.3. Validation: supersonic flow past a circular cylinder

The density contour plots of the IB simulation and ANSYS-Fluent simulation are presented in Fig. 15. The IB simulation is performed on the grid listed in Table 1. Both the plots report the formation of a bow shock and look qualitatively similar although the gradients appear sharper with the Fluent simulations, especially in the wake of the cylinder.

4.3.1. Grid refinement

Plots of C_p, generated using IDW-Upwind and C_f, generated using gradient method, are shown in Fig. 16. The C_p values in

Fig. 16(a) show good convergence, with the medium and fine grids very closely matching with ANSYS-Fluent data. The convergence in C_f is relatively poor though, suggesting that use of even more refined grids may be required. However, as the C_p plots show excellent convergence, the finest grid is used for presenting the comparison with the results from literature and Fluent simulation. It is observed that the noise in the surface data drops with grid refinement. Fig. 16(c) shows the convergence in the error with grid refinement for method A6. The value of C_d calculated using Richardson's extrapolation is 1.56 and the observed order of convergence, p, is 0.7 in this case. A lower order of convergence, *p*, is observed in this case compared to Mach 0.5 flow past the NACA0012 airfoil, which is possibly due to the relatively poor convergence in C_f observed in this case.

4.3.2. Variation in interpolation method

Fig. 17 shows the C_p plots obtained from the three interpolation methods (Section 2.2) that use the smallest stencil (3 × 3). The three methods agree very closely with each other, with the body-fitted grid simulation of ANSYS-Fluent and with the data from literature [42]. The same trend was reported in the case of the flow past the NACA0012 airfoil (Section 4.2).

Fig. 18 compares C_f reconstructed using the shear-stress reconstruction methods (Section 2.2.3), with that from the body-fitted grid simulation in ANSYS-Fluent. As reported in the case of NACA0012 airfoil (Section 4.2), the shear stress determined using the gradient-based method has less noise compared to that
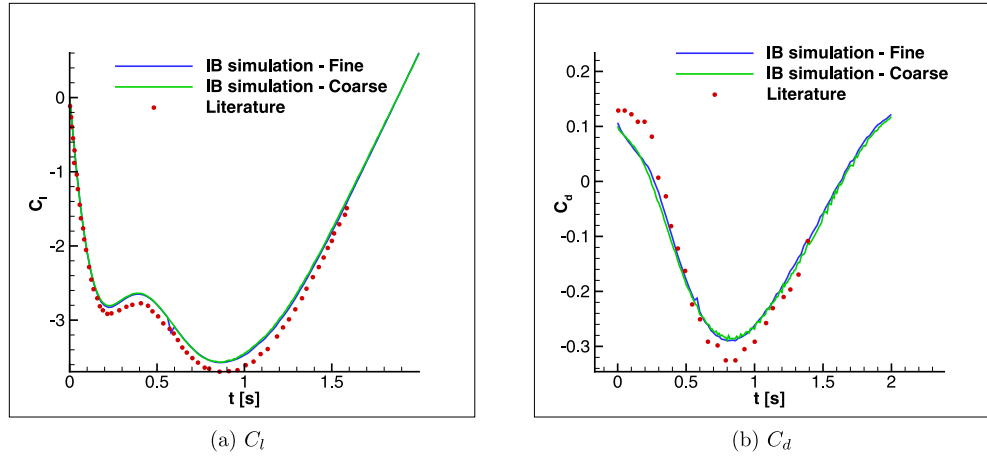
(a) C_l (b) C_d

Fig. 24. Time history of force coefficients for Mach 0.2 flow past a plunging NACA0012 airfoil.

Table 6
Comparison of C_d values for Mach 2.0 flow past a circular cylinder (A1:A6); $C_{d,lit} = 1.54$.

Interpolation	C_d (error)
A1	1.527 (−0.8%)
A2	1.527 (−0.8%)
A3	1.527 (−0.8%)
A4	1.53 (−0.65%)
A5	1.53 (−0.65%)
A6	1.53 (−0.65%)
ANSYS-Fluent	1.537 (−0.19%)

Table 7
Comparison of C_d values for Mach 2.0 flow past a circular cylinder (A1:A6); $C_{d,lit} = 1.54$.

Interpolation	δ error C_d
A1	0.19%
A2	0.19%
A3	0.06%
A4	0.52%
A5	0.52%
A6	0.39%

calculated using the velocity reconstruction method. Table 6 presents C_d predicted by methods A1–A6. The errors in all cases are within 1%, which is excellent. The C_d predictions are slightly better with the use of the velocity gradient reconstruction method for shear stress. Further, the C_d values are insensitive to the choice of pressure reconstruction method. Both these trends were observed in the NACA0012 airfoil case as well. It is interesting to note that even though the shear stress predictions do not compare very well with the ANSYS-Fluent predictions, the computed drag coefficients match. This is possibly due to the fact that the major contribution to drag in this case is from pressure, which shows excellent match with data from literature and ANSYS-Fluent simulations.

4.3.3. Variation in stencil size

Fig. 19 shows a comparison of C_p obtained using the IDW-Upwind method and C_f obtained using velocity gradient reconstruction, for two different interpolation stencil sizes: 3 × 3 and 11 × 11. Larger stencils are, again, seen to smooth the data. Although this being the case, in Fig. 19(b), it is seen that the skin-friction (C_f) predicted is lower for the larger stencil. The reason for this behavior could be that the velocity gradients for this specific flow case are decaying quickly in the direction away from the surface.

Table 7 reports the increase/decrease of error while using a 11 × 11 stencil as compared to a 3 × 3 stencil. This has been described in Section 4.2.3. Here, we see that in all cases, the error is higher for the 11 × 11 stencil. In particular, the error growth in A4–A6 is large, which is consistent with Fig. 19(b) that shows drop in C_f.

4.4. Validation: Mach 3.0 flow past a 10° ramp:

Pressure reconstruction on the surface using the different interpolation methods listed in Section 2.2 are investigated in this

case; shear stress reconstruction is not investigated in this case as the primary objective is to check if the IDW-Upwind method performs better compared to the other pressure interpolation methods as observed in the case of inviscid quasi-1D flow through the convergent–divergent nozzle presented in Section 4.1.2.

4.4.1. Grid refinement

Fig. 20 compares C_p data over the ramp for three grids with data from literature. It is seen that the medium and fine grids produce solutions which are close to each other. Also, there is noise in the C_p data of the coarse grid in the downstream region of the ramp, which reduces with grid refinement.

#### 4.4.2. Variation in interpolation method

Fig. 21 compares the C_p data at the ramp for each of the pressure interpolation methods with that from literature. As seen in the previous validation cases, the three methods perform equally well. Even though this case has an oblique shock present in the domain, the reconstructed surface pressures using IDW-Upwind are not any different from those determined using the IDW and IDW-IP methods. The reason for this is that the viscous effects in the boundary layer smear the rise of pressure over a large region of the wall, as seen in the plots, and the effect of upwinding in the interpolation of pressure becomes insignificant.

4.4.3. Variation in stencil size

Increasing the stencil size reduces noise in the C_p data, as seen in the other validation cases. Fig. 22 shows the C_p plots for this flow case.

4.5. Application: Mach 0.2 flow past plunging NACA0012 airfoil

A temporal convergence study was performed for this case using time steps of 1E-3 s and 5E-4 s. Time-histories of C_l and C_d for

(a) $t/T = 0$

(b) t/T = 0.1

(c) t/T = 0.2

(d) t/T = 0.3
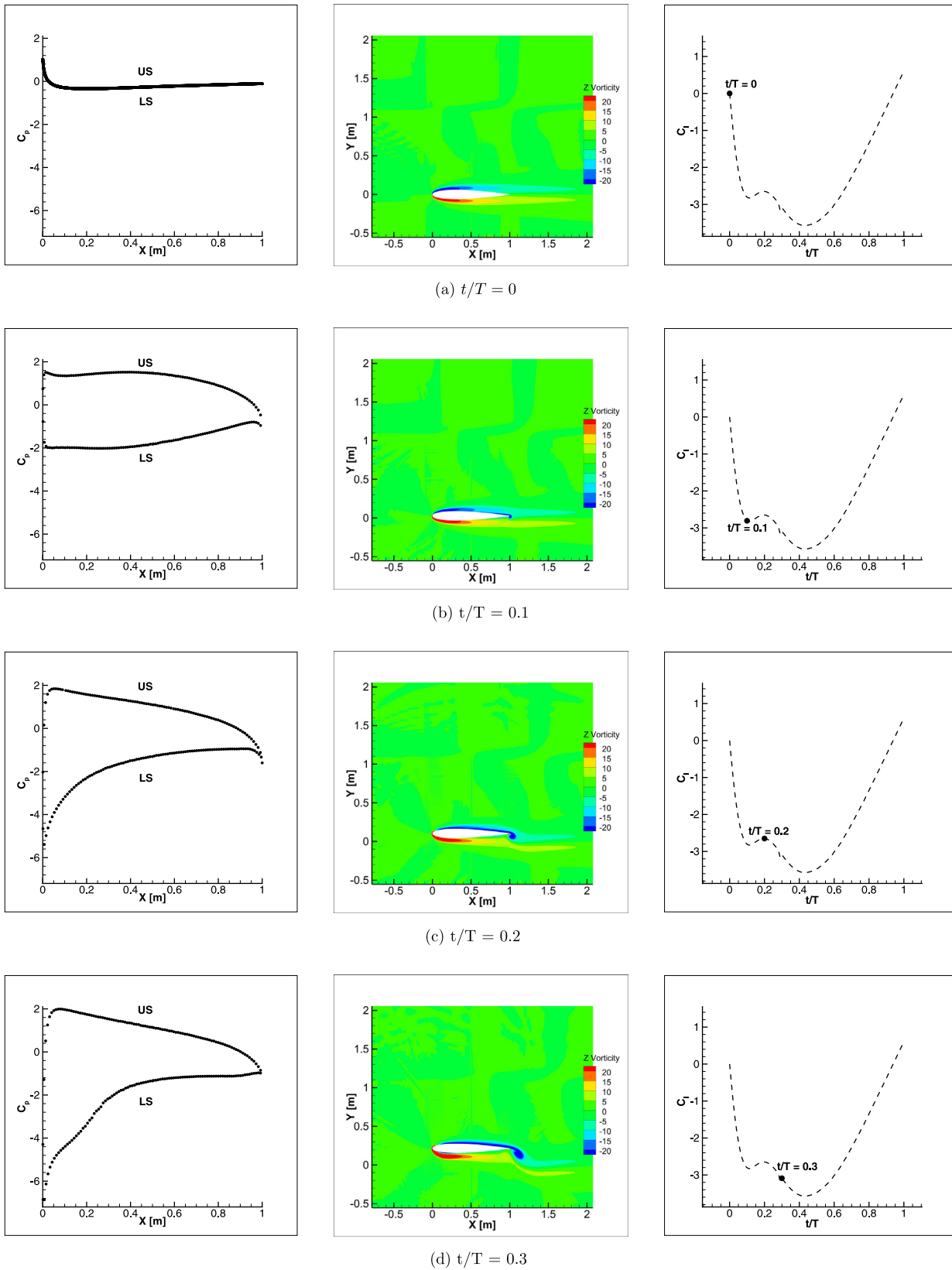
Fig. 25. C_p distribution (left), vorticity contours (middle), and C_l (right) at different times for Mach 0.2 flow past a NACA0012 plunging airfoil: t/T = 0.0–1.0; US – Upper Surface, LS – Lower Surface.

(e) t/T = 0.4

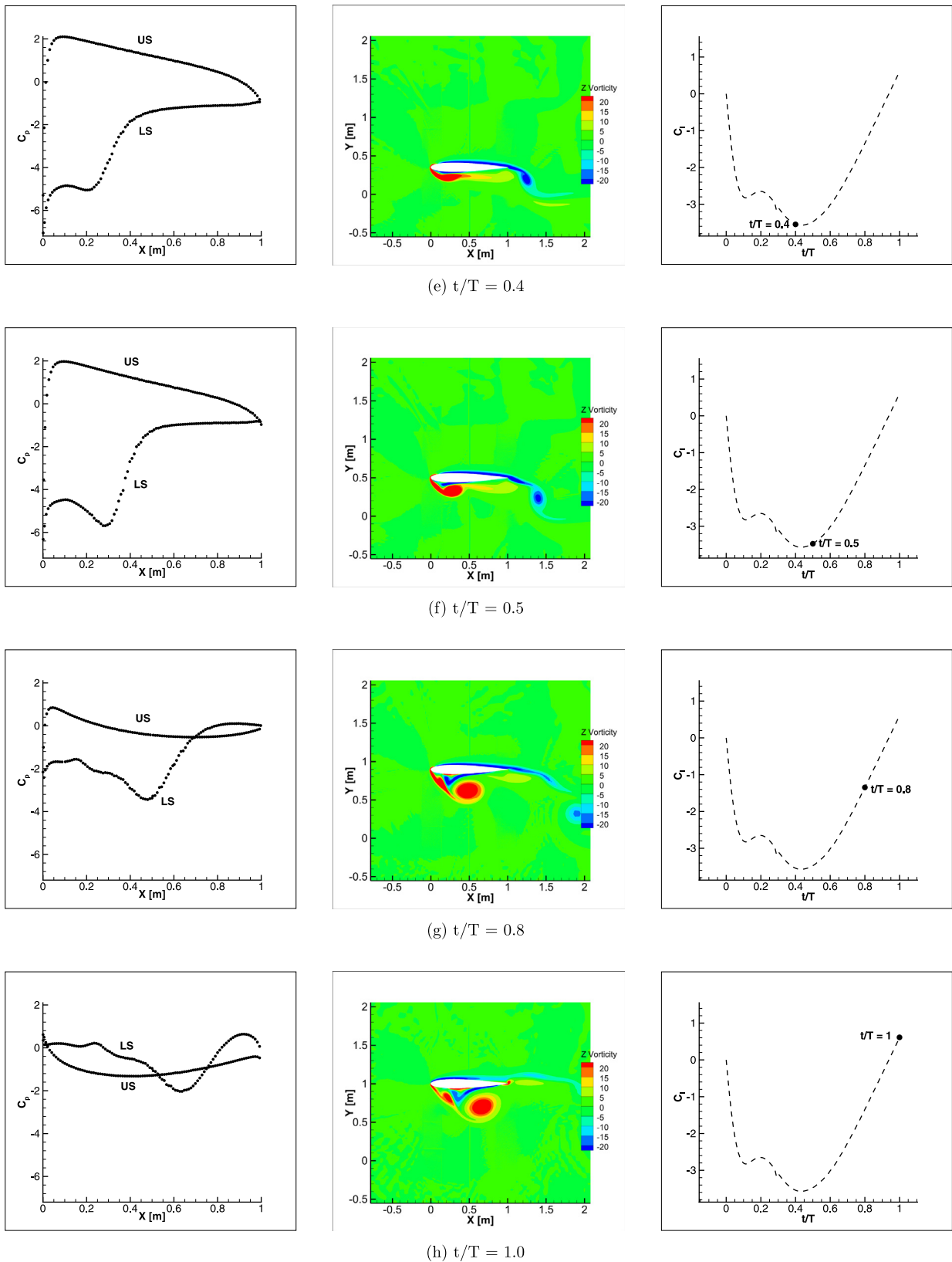(f) t/T = 0.5

(g) t/T = 0.8

(h) t/T = 1.0

Fig. 25. Continued

the two different time steps are shown in Fig. 23. It is observed that the lift and drag coefficients are very close to each other for the two simulations, which suggests that the solutions are time-converged. The following results are presented with the finer time step of 5.0E−4 s.

Time histories of force coefficients plotted in Fig. 24 show that both C_l and C_d predictions using the IBM simulation compare well with literature[40], with the lift predictions being relatively more accurate compared to the drag predictions. Results from simulations using two different grids – 780 × 1400 and 390 × 700 – are shown to check for spurious force oscillations [9]. It is observed that the force coefficients on the coarser grid shows noise in the computed drag-force coefficient. To get further insight into the lift generation during the plunge process, the surface distribution of C_p along the airfoil upper and lower surfaces and the vorticity contours in the domain are plotted at the same time instants in Fig. 25; the lift coefficient at the corresponding instants of time is also shown. The pressure on the airfoil has been calculated using the IDW-Upwind interpolation.

At the start of the heaving motion (Fig. 25a) the airfoil generates no lift and the C_p curves for the upper and lower surfaces are coincident; the vorticity contours also show symmetry about the airfoil chord. In Fig. 25b the airfoil has started to move up and a clockwise vortex can be seen to be rolling down at the trailing edge. The C_p plot indicates that negative lift (as lower surface has lower pressures than upper surface) is generated, which is expected as the airfoil is moving upwards and as such, effectively has a negative angle of attack. The minimum pressure, near the leading edge lower surface, drops further at the next time instant (Fig. 25c), but the overall lift remains similar as the pressure on the upper surface also drops. The lift decreases further (Fig. 25d) as the lower surface pressure drops further. A leading edge vortex on the lower surface is observed in the next frame (Fig. 25e), which results in a sharp drop in the surface pressure around 0.2 c on the lower surface. The vortex is more prominent in Fig. 25f and its centre approximately coincides with the stream-wise location of the pressure trough on the lower surface. The vortex is on the verge of being shed in the next frame (Fig. 25g), and has moved away from the airfoil surface. The airfoil is losing negative lift as its plunge velocity is dropping, and pressures on the lower surface have increased one the whole. At the end of the plunge motion (Fig. 25h), the lower surface pressures are, for the most part, higher compared to the upper surface pressures which results in a positive lift.

5. Conclusions

In this work, three methods of pressure interpolation and two methods of shear stress reconstruction at the immersed surface, vis-à-vis a discrete-forcing immersed-boundary method, have been verified against analytical solution of canonical inviscid flows and validated against CFD data from literature for laminar flow simulations of Mach 0.5 flow past a NACA0012 airfoil, Mach 2.0 flow past a circular cylinder and Mach 3.0 flow past a 10° ramp. Comparisons of the interpolation procedures are presented for surface pressure coefficients, skin friction coefficients and integrated loads, wherein the effect of stencil size on the interpolation methods is also investigated. In general, predictions of surface pressure and shear stress improve - resulting in better accuracy and lesser noise – with grid refinement. Effect of stencil size on the interpolated pressure also indicates that higher stencil size results in smoother surface pressure and shear stress. However, the effect of stencil size on the accuracy of the integrated loads might vary depending on the flow problem being considered, and a case-specific optimal size may exist. Among the interpolation methods for pressure investigated in this work, the IDW and IDW-Upwind methods are seen to re-

sult in less noise in the interpolated surface pressure, compared to the IDW-IP method. Further, the IDW-Upwind method produces the sharpest pressure rise among the interpolation methods for an Euler flow with a normal shock, though a similar result is not obtained for a laminar Mach 3.0 flow past a ramp. This suggests that the additional cost involved in the IDW-Upwind method may not provide any benefit for viscous flows. Considering the fact that the IDW-IP method is based on the interpolation procedure used for the discrete solution forcing, it can be argued that the interpolation strategy used for solution forcing in the neighbourhood of the IB may not be the most suitable method for reconstruction of the data at immersed surface in discrete-forcing immersed-boundary methods. As for the shear stress reconstruction, the gradient-based method produces less noise compared to the velocity interpolation method.

Further, although the interpolation methods presented in this work have been tested on a specific immersed-boundary solver, in principle these can be applied to any direct-forcing type immersed-boundary solver, without much additional programming effort.

The data-reconstruction method proposed in this work, in conjunction with an immersed-boundary approach, can thus be used extensively for the prediction of aerodynamic characteristics of airfoils (including multi-component airfoils, airfoils and with ice-accretion, and airfoils with complicated motion), which can be used for design of airfoils and related studies for small UAVs. Further, the shear-stress reconstruction at the immersed-surface can also be used to detect flow-separation and reattachment, which is useful for flow separation and control related studies. As such, the work presented is very relevant in making (discrete-forcing) immersed-boundary methods more useful for airfoil design studies, flow control in airfoils and also, to understand the fluid dynamics involving intricate airfoil motions such as insect flight.

References

[1] Peskin CS. Flow patterns around heart valves: a numerical method. J Comput Phys 1972;10(2):252–71. doi:10.1016/0021-9991(72)90065-4.

[2] Goldstein D, Handler R, Sirovich L. Modeling a no-slip flow boundary with an external force field. J Comput Phys 1993;105(2):354–66. doi:10.1006/jcph.1993.1081.

[3] Fadlun E, Verzicco R, Orlandi P, Mohd-Yusof J. Combined immersed-boundary finite-difference methods for three-Dimensional complex flow simulations. J Comput Phys 2000;161(1):35–60. doi:10.1006/jcph.2000.6484.

[4] Lai M-C, Peskin CS. An immersed boundary method with formal second-order accuracy and reduced numerical viscosity. J Comput Phys 2000;160(2):705–19. doi:10.1006/jcph.2000.6483.

[5] Mittal R, Iaccarino G. Immersed boundary methods. Annu Rev Fluid Mech 2005;37(1):239–61. doi:10.1146/annurev.fluid.37.061903.175743.

[6] Ghias R, Mittal R, Dong H. A sharp interface immersed boundary method for compressible viscous flows. J Comput Phys 2007;225(1):528–53. doi:10.1016/j.jcp.2006.12.007.

[7] Choi J, Oberoi R, Edwards J, Rosati J. An immersed boundary method for complex incompressible flows. J Comput Phys 2007;224(2):757–84. doi:10.1016/j.jcp.2006.10.032.

[8] Ghosh S, Choi J-I, Edwards JR. Numerical simulations of effects of micro vortex generators using immersed-Boundary methods. AIAA J 2010;48(1):92–103. doi:10.2514/1.40049.

[9] Seo JH, Mittal R. A sharp-interface immersed boundary method with improved mass conservation and reduced spurious pressure oscillations. J Comput Phys 2011;230(19):7347–63. doi:10.1016/j.jcp.2011.06.003.

[10] Lee J, You D. An implicit ghost-cell immersed boundary method for simulations of moving body problems with control of spurious force oscillations. J Comput Phys 2013;233:295–314. doi:10.1016/j.jcp.2012.08.044.

[11] Brehm C, Hader C, Fasel H. A locally stabilized immersed boundary method for the compressible Navier–Stokes equations. J Comput Phys 2015;295:475–504. doi:10.1016/j.jcp.2015.04.023.

[12] Sharma P, Varma D, Ghosh S. Novel vortex generator for mitigation of shock-induced flow separation. J Propuls Power 2016;32(5):1264–74. doi:10.2514/1.B35962.

[13] Varma D, Saurav S, Ghosh S. Flow control in a Mach 4.0 inlet by slotted wedge-shaped vortex generators. In: 33rd AIAA applied aerodynamics conference. Reston, Virginia: American Institute of Aeronautics and Astronautics; 2015. https://doi.org/10.2514/6.2015-2727. https://doi.org/10.2514/6.2015-2727 http://arc.aiaa.org/doi/10.2514/6.2015-2727

[14] Sandhu JPS, Ghosh S, Subramanian S, Sharma P. Evaluation of ramp-type micro vortex generators using swirl center tracking. AIAA J 2018:1–11. doi:10.2514/1.J056796.

[15] Peskin CS, McQueen DM. A three-dimensional computational method for blood flow in the heart I. Immersed elastic fibers in a viscous incompressible fluid. J Comput Phys 1989;81(2):372–405.

[16] Choi J-I, Edwards JR, Rosati JA, Eisner AD. Large eddy simulation of particle re-suspension during a footstep. Aerosol Science and Technology 2011. doi:10.1080/02786826.2011.631613.

[17] Oberoi RC, Choi JI, Edwards JR, Rosati JA, Thornburg J, Rodes CE. Human-induced particle re-suspension in a room. Aerosol Sci Technol 2010. doi:10.1080/02786820903530852.

[18] Ghosh S. An immersed boundary method for simulating the effects of control devices used in Mitigating Shoc boundary layer interactions; 2010. Ph.D. thesis.

[19] Tamaki Y, Imamura T. Turbulent flow simulations of the common research model using immersed boundary method. AIAA Jo 2018;56(6):2271–82. doi:10.2514/1.J056654.

[20] Miller LA, Peskin CS. Flexible clap and fling in tiny insect flight. J Exp Biol 2009;212(19). 3076 LP – 3090. http://jeb.biologists.org/content/212/19/3076.abstract

[21] Ghosh S, Edwards JR, Choi J-I. Numerical simulation of effects of mesoflaps in controlling shock/boundary-layer interactions. J Propuls Power 2012;28(5):955–70. doi:10.2514/1.B34297.

[22] Zheng X, Xue Q, Mittal R, Beilamowicz S. A coupled sharp-Interface immersed boundary-finite-element method for flow-Structure interaction with application to human phonation. J Biomech Eng 2010;132(11):111003. doi:10.1115/1.4002587.

[23] Yang J, Balaras E. An embedded-boundary formulation for large-eddy simulation of turbulent flows interacting with moving boundaries. J Comput Phys 2006;215(1):12–40. doi:10.1016/j.jcp.2005.10.035.

[24] de Tullio M, De Palma P, Iaccarino G, Pascazio G, Napolitano M. An immersed boundary method for compressible flows using local grid refinement. J Comput Phys 2007;225(2):2098–117. doi:10.1016/j.jcp.2007.03.008.

[25] Tseng Y-H, Ferziger JH. A ghost-cell immersed boundary method for flow in complex geometry. J Comput Phys 2003;192(2):593–623. doi:10.1016/j.jcp.2003.07.024.

[26] Mittal R, Dong H, Bozkurttas M, Najjar F, Vargas A, von Loebbecke A. A versatile sharp interface immersed boundary method for incompressible flows with complex boundaries. J Comput Phys 2008;227(10):4825–52. doi:10.1016/j.jcp.2008.01.028.

[27] Peskin CS. Numerical analysis of blood flow in the heart. J Comput Phys 1977;25(3):220–52.

[28] Beyer RP, LeVeque RJ. Analysis of a one-dimensional model for the immersed boundary method. SIAM J Numer Anal 1992;29(2):332–64. doi:10.1137/0729022.

[29] Ghosh S, Choi J-I, Edwards JR. Simulation of shock/boundary-layer interactions with bleed using immersed-boundary methods. J Propuls Power 2010;26(2):203–14. doi:10.2514/1.45297.

[30] Majumdar S, Iaccarino G, Durbin P. Rans solvers with adaptive structured boundary non-conforming grids. In: Annual research briefs, center for turbulence research, Stanford University; 2001. p. 353–466.

[31] Taira K, Colonius T. The immersed boundary method: a projection approach. J Comput Phys 2007;225(2):2118–37. doi:10.1016/j.jcp.2007.03.005.

[32] Uhlmann M. An immersed boundary method with direct forcing for the simulation of particulate flows. J Comput Phys 2005;209(2):448–76.

[33] Roy CJ, Edwards JR. Numerical simulation of a three-dimensional flame/shock wave interaction. AIAA J 2000;38(5):745–54. doi:10.2514/2.1035.

[34] Edwards JR. A low-diffusion flux-splitting scheme for Navier–Stokes calculations. Comput Fluids 1997;26(6):635–59. doi:10.1016/S0045-7930(97)00014-5.

[35] Colella P, Woodward PR. The piecewise parabolic method (PPM) for gas-dynamical simulations. JComputatPhys 1984;54(1):174–201. doi:10.1016/0021-9991(84)90143-8.

[36] Van Leer B. Towards the ultimate conservative difference scheme. v. a second-order sequel to Godunov's method. JComput Phys 1979;32(1):101–36. doi:10.1016/0021-9991(79)90145-1.

[37] van Leer B. Flux-vector splitting for the euler equations. In: Krause E, editor. Eighth international conference on numerical methods in fluid dynamics. Berlin, Heidelberg: Springer Berlin Heidelberg; 1982. p. 507–12.

[38] May G, Woopen M. Test case c1.3: steady flow over the naca0012 airfoil. 2nd international workshop on high-order CFD methods; 2013.

[39] Hung C, MacCormack R. Numerical solutions of supersonic and hypersonic laminar compression corner flows. AIAA J 1976;14(4):475–81.

[40] Persson P-O, Fidkowski C. Test case cl1: heaving and pitching airfoil. 5th international workshop on high-order CFD methods; 2018.

[41] Slater JW. Examining spatial (grid) convergence. https://wwwgrcnasagov/www/wind/valid/tutorial/spatconvhtml 2008;.

[42] Qiu Y, Shu C, Wu J, Sun Y, Yang L, Guo T. A boundary condition-enforced immersed boundary method for compressible viscous flows. Comput Fluids 2016;136:104–13. doi:10.1016/j.compfluid.2016.06.004.